# Unified theoretical framework for mixing state of black carbon

**Authors:** Jiandong Wang[1]*[†], Jiaping Wang[2]*[†], Runlong Cai[3], Chao Liu[1], Jingkun Jiang[4], Wei Nie[2], Jinbo Wang[2], Nobuhiro Moteki[5], Rahul A. Zaveri[6], Xin Huang[2], Nan Ma[7], Ganzhen Chen[1], Zilin Wang[2], Yuzhi Jin[1], Jing Cai[3], Yuxuan Zhang[2], Xuguang Chi[2], Bruna Holanda[8], Jia Xing[4], Tengyu Liu[2], Ximeng Qi[2], Qiaoqiao Wang[7], Christopher Pöhlker[8], Hang Su[8], Yafang Cheng[8], Shuxiao Wang[4], Jiming Hao[4], Meinrat O. Andreae[8, 9, 10], Aijun Ding[2]*

**Affiliations:**
[1]Key Laboratory for Aerosol-Cloud-Precipitation of China Meteorological Administration, School of Atmospheric Physics, Nanjing University of Information Science and Technology, Nanjing 210044, China;
[2]Joint International Research Laboratory of Atmospheric and Earth System Sciences, School of Atmospheric Sciences, Nanjing University, Nanjing, 210023, China;
[3]Institute for Atmospheric and Earth System Research / Physics, Faculty of Science, University of Helsinki, Helsinki, 00014, Finland;
[4]State Key Joint Laboratory of Environment Simulation and Pollution Control, School of Environment, Tsinghua University, Beijing 100084, China;
[5]Department of Earth and Planetary Science, Graduate School of Science, The University of Tokyo, Tokyo, Japan;
[6]Atmospheric Sciences & Global Change Division, Pacific Northwest National Laboratory, Richland, Washington 99352, United States;
[7]Institute for Environmental and Climate Research, Jinan University, 511443, Guangzhou, China.
[8]Max Planck Institute for Chemistry, 55128 Mainz, Germany;
[9]Scripps Institution of Oceanography, University of California San Diego, La Jolla, CA 92093, USA;
[10]Department of Geology and Geophysics, King Saud University, 11451 Riyadh, Saudi Arabia.

[†]These authors contributed equally to this work.
*Corresponding author. Email: dingaj@nju.edu.cn; wangjp@nju.edu.cn; jiandong.wang@nuist.edu.cn

**Abstract:** Black carbon (BC) plays an important role in the climate system due to its strong warming effect, yet the magnitude of this effect is highly uncertain due to the complex mixing state of aerosols. Here we build a unified theoretical framework to describe BC's mixing states, linking dynamic processes to BC coating thickness distribution, and show its self-similarity for sites in diverse environments. The size distribution of BC-containing particles is found to follow an exponential pattern and is independent of BC core size. A mixing state module is established based on this finding and successfully applied in global and regional models, which increases the accuracy of aerosol climate effect estimations. Our theoretical framework can bridge the gap between observation and model simulation in both mixing state description and light absorption quantification.

**This paper is a non-peer reviewed preprint submitted to EarthArXiv.**

**Main Text:**

As a ubiquitous aerosol component, black carbon (BC) is a major contributor to global warming due to its strong light absorption[1–7], which strongly depends on its mixing state[2, 8–15]. Undergoing multiple atmospheric processes, freshly emitted BC can be internally mixed with other aerosol components (i.e., BC coating) and its light absorption is enhanced by the "lensing effect" (1, 16–19). In the real atmosphere, the mixing state of BC-containing particles is a complex property related to several processes, including condensation, coagulation, and deposition. Many studies have characterized mixing state properties from different aspects based on field observations[8, 9, 20–24]. However, the overall effect of these dynamic processes on BC mixing state is not well understood. Moreover, the complexity and diversity of BC mixing states in the real atmosphere cannot be represented in global climate models, and therefore these models generally use simplified schemes, assuming either an internal or external mixture of aerosols[2, 25], leading to a wide range of estimated BC mass absorption cross-sections (MAC) from 3.1 to 18.0 $m^2$/g (at 550 nm) on global average[25, 26]. Therefore, a precise description of BC mixing state becomes the determinant factor of model performance when estimating BC optical properties and radiative forcing.

In this study, we built a theoretical framework linking dynamic processes to BC coating thickness distribution and discovered the self-similarity of BC mixing states, which was verified in eight different observation sites globally. The size distribution of BC-containing particles is found to follow an exponential pattern and to be independent of BC core size. Such self-similarity allows us to greatly simplify the characterization of BC mixing states in both model simulations and field observations. A new mixing state scheme was established for model simulation, which can precisely represent the BC mixing state. Our study bridges the gap between observations and model simulations in both mixing state and light absorption.

Fig. 1 provides a conceptional scheme describing the main physical processes and evolution of aerosols in the atmosphere. After being emitted into the atmosphere, BC particles experience both growth and scavenging progresses continuously, which form a steady-state (27), that is, the particle diameter distribution is approximately steady (although the overall concentration may change). The growth of BC via condensation and coagulation results in an enlarged particle size. During these processes, non-BC materials coat the BC core while the core size remains the same. For clarity, the overall size of BC-containing particle is represented as BC size ($D_p$) and BC core size stands for the diameter of the absorbing core only ($D_c$). To explore the $D_p$ distribution in the atmosphere, a theoretical derivation was performed. We assume a monodisperse aerosol population (consisting of BC cores only) emitted into atmosphere at time zero with diameter of $D_c$ and number of $n(D_c)$. After that, the particles grow in size due to condensation and coagulation. Their diameters reach $D_p$ at time $t$ and the change of particle size $D_p$ with time can be represented as the growth rate ($GR$).

$$\frac{d(D_p)}{dt} = GR \tag{1}$$

The time evolution of $D_p$ can be integrated to give

$$D_p = GR \cdot t + D_c \tag{2}$$

The number of $n(D_p)$ decays due to scavenging process

$$dn(D_p) = -S \cdot n(D_p)dt \tag{3}$$

where $S$ is the scavenging rate. Then, the time evolution of $n(D_p)$ can be integrated as

$$n(D_p) = n(D_c) \cdot e^{-S \cdot t} \tag{4}$$

Based on the steady-state approximation, Eq. 2 and Eq. 4 can be combined, and the size distribution of BC-containing particles in the atmosphere are presented as

$$n(D_p) = n(D_c) \cdot e^{-\frac{S}{GR}(D_p - D_c)} \tag{5}$$

Taking the logarithm on both sides, Eq. 5 becomes

$$ln(n(D_p)) = ln(n(D_c)) - \frac{S}{GR}(D_p - D_c) \tag{6}$$

Eq. 6 shows that for different particle sizes, $ln(n(D_p))$ and $D_p - D_c$ ($\Delta D_p$), which is defined as coating thickness) are in a linear relationship (Fig. 1). The slope $k = \frac{S}{GR}$ is determined by the scavenging rate and the growth rate.

The above derivation demonstrates that the BC coating thickness can be fully described if the slope $k$ and the BC core number-size distribution are known. Based on Eq. 5, the average coating thickness can be derived as $1/k$ (the detailed formula is shown as Eq. M8 in SI). Note that we adopted a simplified derivation in the above theoretical analysis for better understanding. A more rigorous derivation as well as the interpretation of the dependency of $GR$ and $S$ on $D_p$ and time can be found in the SI (theoretical derivation part and Fig. S1). Furthermore, we find that the slope $k$ is independent of $D_p$ and $D_c$, indicating the self-similarity of BC size distributions, that is, BC-containing aerosol with different core sizes should have similar distributions of coating thickness. Such self-similarity allows us to greatly simplify the description of BC mixing states.

We verified our theoretical model by field observations of BC size using the single particle soot photometer (SP2, Droplet Measurement Technologies, USA), which is a well-recognized instrument capable to measure BC mixing state) from eight sites covering different environments globally(24, 28, 29). As presented in Fig. 2, the BC size distribution follows an exponential law at all sites despite their different regions and properties (e.g., urban, regional background), which agrees well with our theoretical model. The linear regression yields the slopes, $k$, ranging from 0.008 to 0.020, providing a useful parameter to quantify BC size distribution and its absorption enhancement.

The $D_p$ distributions with different BC core size ranges (110–120 nm, 120–130 nm, 130–140 nm, and 140–150 nm) from SP2 measurements at four sites are presented in Fig. 3. At all four sites,

approximately the same slopes of $ln(n(D_p)) \sim D_p$ can be observed for the BC size distribution, independent of $D_c$, supporting Eq. 6. This phenomenon indicates that the self-similarity of BC size distribution is ubiquitous in the real atmosphere.

5 The light absorption calculation of BC can be simplified based on our theory, which is applicable to climate models and chemical transport models. The absorption enhancement factor, $E_{abs}$, is a widely used parameter to represent BC light absorption amplification. As shown in Fig. S2, the relationship between $E_{abs}$ and $\Delta D_p$ is approximately linear when $\Delta D_p$ is small. Therefore, the BC coating thickness distribution can be replaced by a monodisperse coating thickness, $1/k$, when 10 calculating the black carbon absorption (a detailed demonstration can be found in SI). Light absorption coefficients over all $D_p$ and with mean $D_p$ show a good agreement (exhibited in Fig. S3), which further validates this simplification. Hence, this approximation can be applied directly in global and regional models for optical estimation.

15 Based on the above findings, we established a new mixing state module and applied it in a global climate model (CESM-CAM6) and a chemical transport model (WRF-chem) as examples. Model simulations of $E_{abs}$ and BC direct radiative forcing (DRF) were performed using these two models alternatively with our new module and the conventional assumption of mixing state. Comparing the results with observation data shown in Fig. 4(A), the simulated $E_{abs}$ using the 20 conventional assumption of fully internal mixing (2 to 3.5) is significantly higher than observations (1.0 to 1.7). Using our new module, the calculated $E_{abs}$ is around 1.4, which agrees well with observation data, demonstrating the good performance of our mixing state description in $E_{abs}$ quantification. As for BC-caused DRF, the global average DRF estimated with CAM decreases from 0.37 W m$^{-2}$ to 0.17 W m$^{-2}$ by using the new module, in agreement with the recently-25 found overestimation of radiative warming by BC in global climate models, largely due to the treatment of aerosol mixing state (*30*).

We built a unified theoretical framework based on a steady-state assumption to describe the complex mixing state of BC and found its self-similarity confirmed across a wide range of field ob-30 servation sites. Our findings link the representation of particle diameter (from field observations) and dynamic parameters (generally used in models), making observational data applicable in model simulations. This unified theoretical framework reduces the dimension of mixing state descriptions. The mixing state module established in this study can be embedded in various types of atmospheric models and efficiently increases the accuracy of aerosol climate effect estima-35 tions without increasing computational complexity.

**References**

1. M. Z. Jacobson, Strong radiative heating due to the mixing state of black carbon in atmospheric aerosols. *Nature*. **409**, 695–697 (2001).

2. T. C. Bond, S. J. Doherty, D. W. Fahey, P. M. Forster, T. Berntsen, B. J. DeAngelo, M. G. Flanner, S. Ghan, B. Kaercher, D. Koch, S. Kinne, Y. Kondo, P. K. Quinn, M. C. Sarofim, M. G. Schultz, M. Schulz, C. Venkataraman, H. Zhang, S. Zhang, N. Bellouin, S. K. Guttikunda, P. K. Hopke, M. Z. Jacobson, J. W. Kaiser, Z. Klimont, U. Lohmann, J. P. Schwarz, D. Shindell, T. Storelvmo, S. G. Warren, C. S. Zender, Bounding the role of black carbon in the climate system: A scientific assessment. *Journal of Geophysical Research-Atmospheres*. **118**, 5380–5552 (2013).

3. V. Ramanathan, G. Carmichael, Global and regional climate changes due to black carbon. *Nature Geoscience*. **1**, 221–227 (2008).

4. M. O. Andreae, V. Ramanathan, Climate's Dark Forcings. *Science*. **340**, 280–281 (2013).

5. M. V. Ramana, V. Ramanathan, Y. Feng, S. C. Yoon, S. W. Kim, G. R. Carmichael, J. J. Schauer, Warming influenced by the ratio of black carbon to sulphate and the black-carbon source. *Nature Geosci*. **3**, 542–545 (2010).

6. J. R. McConnell, R. Edwards, G. L. Kok, M. G. Flanner, C. S. Zender, E. S. Saltzman, J. R. Banta, D. R. Pasteris, M. M. Carter, J. D. W. Kahl, 20th-century industrial black carbon emissions altered arctic climate forcing. *Science*. **317**, 1381–1384 (2007).

7. M. O. Andreae, The dark side of aerosols. *Nature*. **409**, 671–672 (2001).

8. N. Riemer, A. P. Ault, M. West, R. L. Craig, J. H. Curtis, Aerosol Mixing State: Measurements, Modeling, and Impacts. *Rev. Geophys.* **57**, 187–249 (2019).

9. C. D. Cappa, T. B. Onasch, P. Massoli, D. R. Worsnop, T. S. Bates, E. S. Cross, P. Davidovits, J. Hakala, K. L. Hayden, B. T. Jobson, K. R. Kolesar, D. A. Lack, B. M. Lerner, S. M. Li, D. Mellon, I. Nuaaman, J. S. Olfert, T. Petaja, P. K. Quinn, C. Song, R. Subramanian, E. J. Williams, R. A. Zaveri, Radiative Absorption Enhancements Due to the Mixing State of Atmospheric Black Carbon. *Science*. **337**, 1078–1081 (2012).

10. L. Fierce, T. B. Onasch, C. D. Cappa, C. Mazzoleni, S. China, J. Bhandari, P. Davidovits, D. A. Fischer, T. Helgestad, A. T. Lambe, A. J. Sedlacek, G. D. Smith, L. Wolff, Radiative absorption enhancements by black carbon controlled by particle-to-particle heterogeneity in composition. *Proceedings of the National Academy of Sciences*. **117**, 5196 (2020).

11. H. Matsui, D. S. Hamilton, N. M. Mahowald, Black carbon radiative effects highly sensitive to emitted particle size when resolving mixing-state diversity. *Nat Commun*. **9**, 3446 (2018).

12. D. T. Liu, J. Whitehead, M. R. Alfarra, E. Reyes-Villegas, D. V. Spracklen, C. L. Reddington, S. F. Kong, P. I. Williams, Y. C. Ting, S. Haslett, J. W. Taylor, M. J. Flynn, W. T. Morgan, G. McFiggans, H. Coe, J. D. Allan, Black-carbon absorption enhancement in the atmosphere determined by particle mixing state. *Nat. Geosci.* **10**, 184-U132 (2017).

13. S. Liu, A. C. Aiken, K. Gorkowski, M. K. Dubey, C. D. Cappa, L. R. Williams, S. C. Herndon, P. Massoli, E. C. Fortner, P. S. Chhabra, W. A. Brooks, T. B. Onasch, J. T. Jayne, D. R. Worsnop, S. China, N. Sharma, C. Mazzoleni, L. Xu, N. L. Ng, D. Liu, J. D. Allan, J. D. Lee, Z. L. Fleming, C. Mohr, P. Zotter, S. Szidat, A. S. H. Prevot, Enhanced light absorption by mixed source black and brown carbon particles in UK winter. *Nat Commun*. **6** (2015), doi:10.1038/ncomms9435.

14. P. Stier, J. H. Seinfeld, S. Kinne, J. Feichter, O. Boucher, Impact of nonabsorbing anthropogenic aerosols on clear-sky atmospheric absorption. *Journal of Geophysical Research-Atmospheres*. **111** (2006), doi:10.1029/2006jd007147.

15.     A. Virkkula, Modeled source apportionment of black carbon particles coated with a light-scattering shell. *Atmos. Meas. Tech.* **14**, 3707–3719 (2021).

16.     T. C. Bond, R. W. Bergstrom, Light absorption by carbonaceous particles: An investigative review. *Aerosol Science and Technology*. **40**, 27–67 (2006).

17.     J. Peng, M. Hu, S. Guo, Z. Du, J. Zheng, D. Shang, M. Levy Zamora, L. Zeng, M. Shao, Y.-S. Wu, J. Zheng, Y. Wang, C. R. Glen, D. R. Collins, M. J. Molina, R. Zhang, Markedly enhanced absorption and direct radiative forcing of black carbon under polluted urban environments. *Proceedings of the National Academy of Sciences*. **113**, 4266 (2016).

18.     R. K. Chakrabarty, W. R. Heinson, Scaling Laws for Light Absorption Enhancement Due to Nonrefractory Coating of Atmospheric Black Carbon Aerosol. *Phys. Rev. Lett.* **121**, 6 (2018).

19.     Y. Wang, W. Li, J. Huang, L. Liu, Y. Pang, C. He, F. Liu, D. Liu, L. Bi, X. Zhang, Z. Shi, Nonlinear Enhancement of Radiative Absorption by Black Carbon in Response to Particle Mixing Structure. *Geophysical Research Letters*. **48** (2021), doi:10.1029/2021GL096437.

20.     R. S. Gao, J. P. Schwarz, K. K. Kelly, D. W. Fahey, L. A. Watts, T. L. Thompson, J. R. Spackman, J. G. Slowik, E. S. Cross, J.-H. Han, P. Davidovits, T. B. Onasch, D. R. Worsnop, A Novel Method for Estimating Light-Scattering Properties of Soot Aerosols Using a Modified Single-Particle Soot Photometer. *Aerosol Science and Technology*. **41**, 125–135 (2007).

21.     R. M. Healy, N. Riemer, J. C. Wenger, M. Murphy, M. West, L. Poulain, A. Wiedensohler, I. P. O'Connor, E. McGillicuddy, J. R. Sodeau, G. J. Evans, Single particle diversity and mixing state measurements. *Atmos. Chem. Phys.* **14**, 6289–6299 (2014).

22.     C. L. Reddington, G. McMeeking, G. W. Mann, H. Coe, M. G. Frontoso, D. Liu, M. Flynn, D. V. Spracklen, K. S. Carslaw, The mass and number size distributions of black carbon aerosol over Europe. *Atmos. Chem. Phys.* **13**, 4917–4939 (2013).

23.     H. Che, H. Zhao, Y. Wu, X. Xia, J. Zhu, O. Dubovik, V. Estelles, Y. Ma, Y. Wang, H. Wang, Y. Wang, X. Zhang, G. Shi, Application of aerosol optical properties to estimate aerosol type from ground-based remote sensing observation at urban area of northeastern China. *Journal of Atmospheric and Solar-Terrestrial Physics*. **132**, 37–47 (2015).

24.     R. A. Zaveri, W. J. Shaw, D. J. Cziczo, B. Schmid, R. A. Ferrare, M. L. Alexander, M. Alexandrov, R. J. Alvarez, W. P. Arnott, D. B. Atkinson, S. Baidar, R. M. Banta, J. C. Barnard, J. Beranek, L. K. Berg, F. Brechtel, W. A. Brewer, J. F. Cahill, B. Cairns, C. D. Cappa, D. Chand, S. China, J. M. Comstock, M. K. Dubey, R. C. Easter, M. H. Erickson, J. D. Fast, C. Floerchinger, B. A. Flowers, E. Fortner, J. S. Gaffney, M. K. Gilles, K. Gorkowski, W. I. Gustafson, M. Gyawali, J. Hair, R. M. Hardesty, J. W. Harworth, S. Herndon, N. Hiranuma, C. Hostetler, J. M. Hubbe, J. T. Jayne, H. Jeong, B. T. Jobson, E. I. Kassianov, L. I. Kleinman, C. Kluzek, B. Knighton, K. R. Kolesar, C. Kuang, A. Kubátová, A. O. Langford, A. Laskin, N. Laulainen, R. D. Marchbanks, C. Mazzoleni, F. Mei, R. C. Moffet, D. Nelson, M. D. Obland, H. Oetjen, T. B. Onasch, I. Ortega, M. Ottaviani, M. Pekour, K. A. Prather, J. G. Radney, R. R. Rogers, S. P. Sandberg, A. Sedlacek, C. J. Senff, G. Senum, A. Setyan, J. E. Shilling, M. Shrivastava, C. Song, S. R. Springston, R. Subramanian, K. Suski, J. Tomlinson, R. Volkamer, H. W. Wallace, J. Wang, A. M. Weickmann, D. R. Worsnop, X. Y. Yu, A. Zelenyuk, Q. Zhang, Overview of the 2010 Carbonaceous Aerosols and Radiative Effects Study (CARES). *Atmos. Chem. Phys.* **12**, 7647–7687 (2012).

25.     J. Gliß, A. Mortier, M. Schulz, E. Andrews, Y. Balkanski, S. E. Bauer, A. M. K. Benedictow, H. Bian, R. Checa-Garcia, M. Chin, P. Ginoux, J. J. Griesfeller, A. Heckel, Z. Kipling, A. Kirkevåg, H. Kokkola, P. Laj, P. Le Sager, M. T. Lund, C. Lund Myhre, H. Matsui, G. Myhre, D. Neubauer, T. van Noije, P. North, D. J. L. Olivié, S. Rémy, L. Sogacheva, T. Takemura, K. Tsigaridis, S. G. Tsyro, AeroCom phase III multi-model evaluation of the aerosol life cycle and

optical properties using ground- and space-based remote sensing as well as surface in situ observations. *Atmos. Chem. Phys.* **21**, 87–128 (2021).

26.     M. Z. Jacobson, Investigating cloud absorption effects: Global absorption properties of black carbon, tar balls, and soil dust in clouds and aerosols. *Journal of Geophysical Research-Atmospheres*. **117** (2012), doi:10.1029/2011jd017218.

27.     W. C. Hinds, *Aerosol technology: properties, behavior, and measurement of airborne particles* (Wiley, New York, 2nd ed., 1999).

28.     N. Moteki, Y. Kondo, K. Adachi, Identification by single-particle soot photometer of black carbon particles attached to other particles: Laboratory experiments and ground observations in Tokyo. *Journal of Geophysical Research-Atmospheres*. **119**, 1031–1043 (2014).

29.     Y. Zhang, Q. Zhang, Y. Cheng, H. Su, H. Li, M. Li, X. Zhang, A. Ding, K. He, Amplification of light absorption of black carbon associated with air pollution. *Atmos. Chem. Phys.* **18**, 9879–9896 (2018).

30.     H. Brown, X. Liu, R. Pokhrel, S. Murphy, Z. Lu, R. Saleh, T. Mielonen, H. Kokkola, T. Bergman, G. Myhre, R. B. Skeie, D. Watson-Paris, P. Stier, B. Johnson, N. Bellouin, M. Schulz, V. Vakkari, J. P. Beukes, P. G. van Zyl, S. Liu, D. Chand, Biomass burning aerosols in most climate models are too absorbing. *Nat Commun*. **12**, 277 (2021).

31.     A. Knox, G. J. Evans, J. R. Brook, X. Yao, C. H. Jeong, K. J. Godri, K. Sabaliauskas, J. G. Slowik, Mass Absorption Cross-Section of Ambient Black Carbon Aerosol in Relation to Chemical Age. *Aerosol Science and Technology*. **43**, 522–532 (2009).

32.     D. A. Lack, J. M. Langridge, R. Bahreini, C. D. Cappa, A. M. Middlebrook, J. P. Schwarz, Brown carbon and internal mixing in biomass burning particles. *Proceedings of the National Academy of Sciences of the United States of America*. **109**, 14802–14807 (2012).

33.     S. Ueda, T. Nakayama, F. Taketani, K. Adachi, A. Matsuki, Y. Iwamoto, Y. Sadanaga, Y. Matsumi, Light absorption and morphological properties of soot-containing aerosols observed at an East Asian outflow site, Noto Peninsula, Japan. *Atmos. Chem. Phys.* **16**, 2525–2541 (2016).

34.     C. D. Cappa, X. Zhang, L. M. Russell, S. Collier, A. K. Y. Lee, C.-L. Chen, R. Betha, S. Chen, J. Liu, D. J. Price, K. J. Sanchez, G. R. McMeeking, L. R. Williams, T. B. Onasch, D. R. Worsnop, J. Abbatt, Q. Zhang, Light Absorption by Ambient Black and Brown Carbon and its Dependence on Black Carbon Coating State for Two California, USA, Cities in Winter and Summer. *J. Geophys. Res. Atmos.* **124**, 1550–1577 (2019).

35.     Y. Ma, C. Huang, H. Jabbour, Z. Zheng, Y. Wang, Y. Jiang, W. Zhu, X. Ge, S. Collier, J. Zheng, Mixing state and light absorption enhancement of black carbon aerosols in summertime Nanjing, China. *Atmospheric Environment*. **222**, 117141 (2020).

36.     A. Ding, W. Nie, X. Huang, X. Chi, J. Sun, V.-M. Kerminen, Z. Xu, W. Guo, T. Petäjä, X. Yang, M. Kulmala, C. Fu, Long-term observation of air pollution-weather/climate interactions at the SORPES station: a review and outlook. *Frontiers of Environmental Science & Engineering*. **10**, 15- (2016).

37.     A. J. Ding, C. B. Fu, X. Q. Yang, J. N. Sun, T. Petäjä, V. M. Kerminen, T. Wang, Y. Xie, E. Herrmann, L. F. Zheng, W. Nie, Q. Liu, X. L. Wei, M. Kulmala, Intense atmospheric pollution modifies weather: a case of mixed biomass burning with fossil fuel combustion pollution in eastern China. *Atmos. Chem. Phys.* **13**, 10545–10554 (2013).

38.     J. P. Schwarz, R. S. Gao, D. W. Fahey, D. S. Thomson, L. A. Watts, J. C. Wilson, J. M. Reeves, M. Darbeheshti, D. G. Baumgardner, G. L. Kok, S. H. Chung, M. Schulz, J. Hendricks, A. Lauer, B. Kärcher, J. G. Slowik, K. H. Rosenlof, T. L. Thompson, A. O. Langford, M. Loewenstein, K. C. Aikin, Single-particle measurements of midlatitude black carbon and light-scattering aerosols from the boundary layer to the lower stratosphere. *J. Geophys. Res.* **111**, D16207 (2006).

39.     T. C. Bond, G. Habib, R. W. Bergstrom, Limitations in the enhancement of visible light absorption due to mixing state. *J. Geophys. Res.-Atmos.* **111**, 13 (2006).

40.     M. Gysel, M. Laborde, J. S. Olfert, R. Subramanian, A. J. Gröhn, Effective density of Aquadag and fullerene soot black carbon reference materials used for SP2 calibration. *Atmos. Meas. Tech.* **4**, 2851–2858 (2011).

41.     M. Schulz, C. Textor, S. Kinne, Y. Balkanski, S. Bauer, T. Berntsen, T. Berglen, O. Boucher, F. Dentener, S. Guibert, I. S. A. Isaksen, T. Iversen, D. Koch, A. Kirkevag, X. Liu, V. Montanaro, G. Myhre, J. E. Penner, G. Pitari, S. Reddy, O. Seland, P. Stier, T. Takemura, Radiative forcing by aerosols as derived from the AeroCom present-day and pre-industrial simulations. *Atmospheric Chemistry and Physics*. **6**, 5225–5246 (2006).

42.     G. Brasseur, D. Hauglustaine, S. Walters, P. Rasch, J. Müller, C. Granier, X. Tie, MOZART, a global chemical transport model for ozone and related chemical tracers: 1. Model description. *Journal of Geophysical Research: Atmospheres*. **103**, 28265–28289 (1998).

43.     G. A. Grell, S. E. Peckham, R. Schmitz, S. A. McKeen, G. Frost, W. C. Skamarock, B. Eder, Fully coupled "online" chemistry within the WRF model. *Atmos Environ*. **39**, 6957–6975 (2005).

44.     J. C. Barnard, J. D. Fast, G. Paredes-Miranda, W. P. Arnott, A. Laskin, Technical Note: Evaluation of the WRF-Chem "Aerosol Chemical to Aerosol Optical Properties" Module using data from the MILAGRO campaign. *Atmos Chem Phys*. **10**, 7325–7340 (2010).

45.     X. Huang, Y. Song, C. Zhao, X. Cai, H. Zhang, T. Zhu, Direct Radiative Effect by Multicomponent Aerosol over China*. *Journal of Climate*. **28**, 3472–3495 (2015).

46.     M. J. Iacono, J. S. Delamere, E. J. Mlawer, M. W. Shephard, S. A. Clough, W. D. Collins, *Journal of Geophysical Research: Atmospheres*, in press, doi:10.1029/2008JD009944.

47.     M. Li, Q. Zhang, J. Kurokawa, J.-H. Woo, K. He, Z. Lu, T. Ohara, Y. Song, D. G. Streets, G. R. Carmichael, Y. Cheng, C. Hong, H. Huo, X. Jiang, S. Kang, F. Liu, H. Su, B. Zheng, MIX: a mosaic Asian anthropogenic emission inventory under the international collaboration framework of the MICS-Asia and HTAP. *Atmos. Chem. Phys.* **17**, 935–963 (2017).

48.     R. A. Zaveri, R. C. Easter, J. D. Fast, L. K. Peters, Model for Simulating Aerosol Interactions and Chemistry (MOSAIC). *J. Geophys. Res.* **113**, D13204 (2008).

**Author Contributions:** J.D.W., J.P.W., and A.J.D. conceived and performed the research; R.L.C. supported theoretical analysis; J.B.W., X.G.C., B.H., N.Moteki, R.A.Z., P.C., N.Ma, Y.X.Z., and Q.Q.W. provided observational data; Y.Z.J., C.L., G.Z.C., Z.L.W. supported the model simulation; J.P.W. and J.D.W. wrote the manuscript; M.O.A. and A.J.D. discussed the results and revised the manuscript; J.K.J, W.N, X.H., J.C., R.A.Z., Y.F.C., H.S., J.X., T.Y.L., X.M.Q., S.X.W. and J.M.H. commented on the manuscript.

**Competing interests:** Authors declare that they have no competing interests.

**Data and materials availability:** All data needed to evaluate the conclusions in the paper are present in the main text or the supplementary materials. Additional data related to this paper may be requested from the authors.
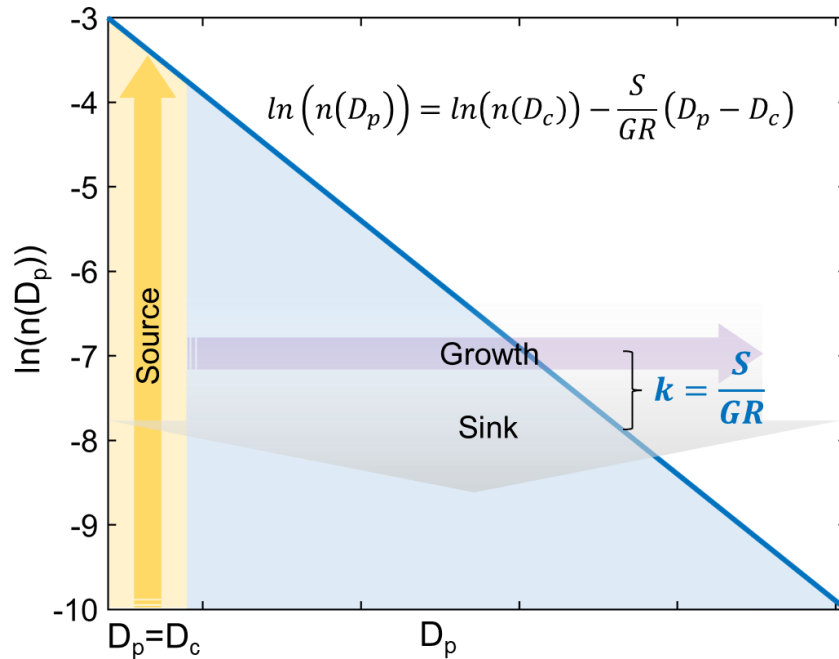
$$ln\left(n(D_p)\right) = ln(n(D_c)) - \frac{S}{GR}(D_p - D_c)$$

**Fig. 1 Similarity of BC size distribution controlled by combined effects of growth and sink.**
The yellow shaded area and arrow show the emission source of BC where $D_c$ is approximately equal to $D_p$. The blue shaded area and line represent the size distribution of $D_p$ controlled by growth (purple arrow) and sink (grey arrow) processes. The slope of the blue line equals to $-\frac{S}{GR}$ in a $ln(n(D_p))$-$D_p$ coordinate system.
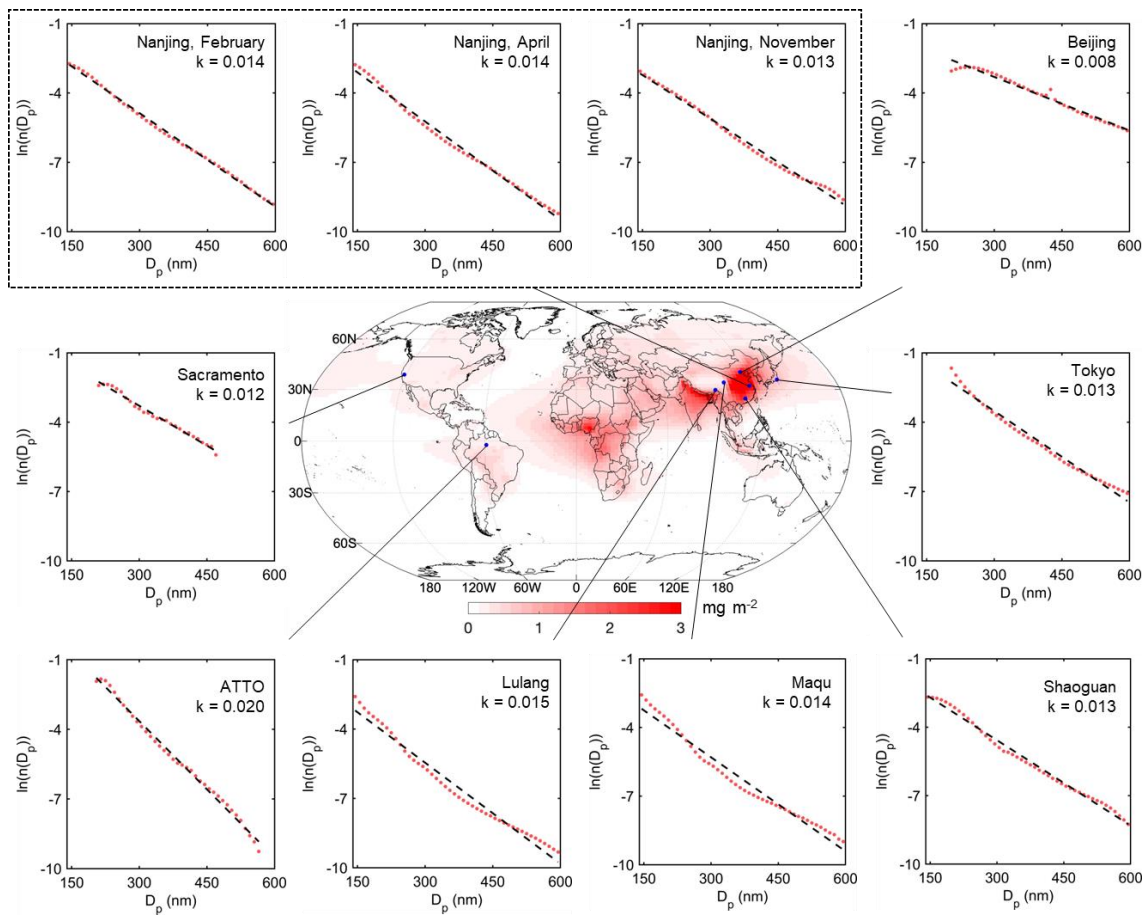
**Fig. 2 Exponent distribution of BC size distributions from field measurements using single particle soot photometers (SP2) at different sites.** The red dots and black lines represent the normalized size distribution of $D_p$ and linear regression, respectively. Observations in Nanjing were conducted in different seasons. Data in Lulang and Maqu were observed over the Tibetan Plateau in spring 2021. Observations in Shaoguan, Beijing(*29*), Tokyo(*28*), Sacramento(*24*), and Amazon Tall Tower Observatory (ATTO) were performed in December 2020, November 2014, August 2012, June 2010, and October 2019, respectively. The map shows simulated BC radiative forcing at top of atmosphere (TOA).
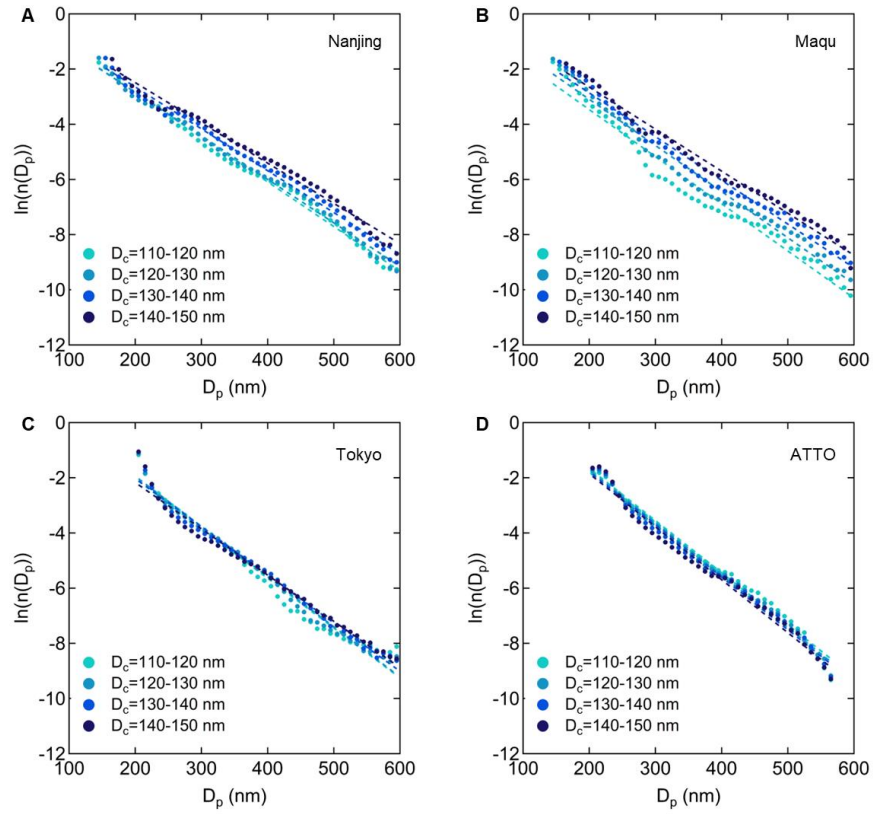
**Fig. 3 BC size distributions with different $D_c$ ranges from SP2 observations at four sites.**
Circles are BC $D_p$ distributions with four selected $D_c$ ranges. Dashed lines represent the linear regression of each distribution. $n(D_p)$ with each $D_c$ range normalized.
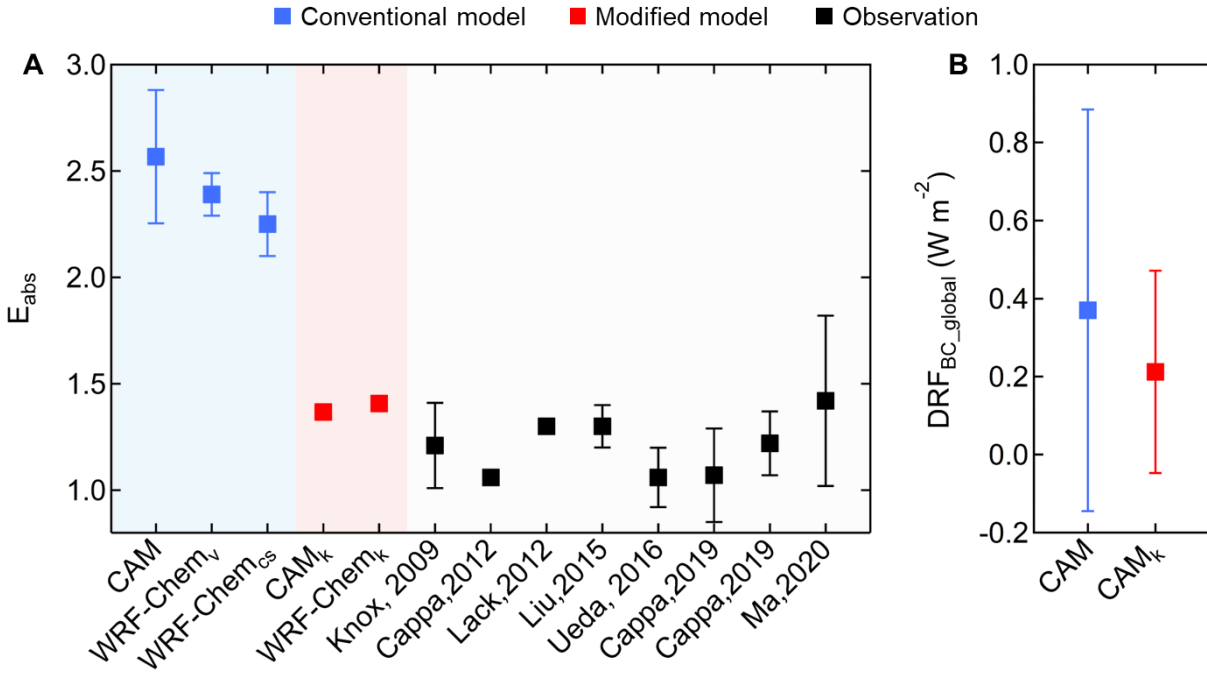
5

**Fig. 4 Model simulated (A) BC absorption enhancement and (B) BC direct radiative forcing (DRF) using the new scheme in this study and the conventional scheme.** The blue and red squares with error bars represent the simulated global average values (± standard deviation) using the conventional scheme and the new scheme, respectively. WRF-Chem$_v$ and WRF-Chem$_{cs}$ stand for WRF-Chem simulations with volume mixing and core-shell mode, respectively. The black squares with error bars (standard deviation) in (A) are $E_{abs}$ observed using the thermodenuder (TD) method at different sites obtained from previous studies(*9, 13, 31–35*). There are two exceptions, which are Knox et al., 2009 (*31*) and Ueda et al., 2016 (*33*). The error bars in Knox et al., 2009 (*31*) represent the $E_{abs}$ of aerosol with different age categories and the error bars in Ueda et al., 2016 (*33*) cover the 25$^{th}$-75$^{th}$ percentiles. The E$_{abs}$ reported in Cappa et al., 2019 (*34*) were observed in two cities (Fresno and Fontana, California, respectively).

**Supplementary Information**

**Materials and Methods**
<u>Theoretical derivation:</u>

The theoretical derivation in the main text is based on Lagrangian coordinate system in $D_p$ space (in Lagrangian coordinates, the $D_p$ distribution for an aerosol population is tracked), which is more intuitive. A more rigorous expression can also be performed using an Eulerian coordinate system in $D_p$ space (in which the number concentration of aerosols in a specific $D_p$ bin is tracked). The general dynamic equation for aerosol number concentration $n(= dN / dD_p)$ in the accumulation mode is,

$$\frac{\partial n(D_p)}{\partial t} + R_{emis} + GR(D_p) \cdot \frac{\partial}{\partial d_p} n(D_p) + S(D_p) \cdot n(D_p) = 0 \qquad (M1)$$

where the second, third and fourth terms represent the impact of emission, growth, and scavenging processes. The growth rate of bins in the accumulation mode is related to the particle diameter, thus $GR(D_p)$ is used. Further, the scavenging rate is also related to the particle diameter and $S(D_p)$ is used to represent the scavenging rate of $D_p$.

For size bins without emission, $R_{emis} = 0$, and Eq. M1 could be simplified as

$$\frac{\partial n(D_p)}{\partial t} + GR(D_p) \cdot \frac{\partial}{\partial D_p} n(D_p) + S(D_p) \cdot n(D_p) = 0 \qquad (M2)$$

Based on the steady-state approximation, $n(D_p)$ does not vary much with time. Thus,

$$\frac{\partial n(D_p)}{\partial t} = 0 \qquad (M3)$$

Combining Eq. M2 and Eq. M3, we obtain,

$$GR(D_p) \cdot \frac{\partial}{\partial D_p} (n(D_p)) = -S(D_p) \cdot n(D_p) \qquad (M4)$$

Therefore,

$$\frac{-S(D_p)}{GR(D_p)} = \frac{\frac{\partial}{\partial D_p} n(D_p)}{n(D_p)} \qquad (M5)$$

$$= \frac{\partial}{\partial D_p} ln(n(D_p))$$

To get the analytical equation, we assume $S$ and $GR$ follow a power-law dependence of $D_p$, $S \sim D_p{}^a$, $GR \sim D_p{}^b$,

$$ln(n(D_p)) = ln(n(D_c)) - \frac{S}{(a-b+1) \cdot GR} \cdot (D_p^{(a-b+1)} - D_c^{(a-b+1)}) \qquad (M6)$$

The $D_p$ distribution with different relationships between $a$ and $b$ is shown in Fig. S1. The derivation in the main text can be considered as a special case when $a=0$ and $b=0$. Our field observation results (Fig. 2) confirm that $ln(n(D_p))$ and $D_c$ are in a linear relationship and indicate that $a \sim b$ in Eq. M6.

In addition to the dependency of $GR$ and $S$ on $D_p$, the variations of $GR$ and $S$ as a function of time should also be considered. The lifetime of BC aerosols is 3-10 days. Therefore, long-term variations of $GR$ and $S$, such as seasonal variation, do not affect the assumption of steady-state and our theoretical framework is applicable. The suitability of this theory under the influence of short-term periodical variations of $GR$ and $S$ (most importantly the diurnal variation) is discussed here.

$GR$ and $S$ are assumed to have a periodical variation with cycling time of $\tau$, that is,

$$\int_{t}^{t+\tau} GR(t)dt = \overline{GR} \cdot \tau \tag{M7}$$

$$\int_{t}^{t+\tau} S(t)dt = \overline{S} \cdot \tau \tag{M8}$$

Hence, Eq. 2 and Eq. 4 can be represented as Eq. M9 and Eq. M10, respectively.

$$\Delta D_p = \int_{t}^{t+\tau} GR(t)dt \tag{M9}$$
$$= \overline{GR} \cdot \tau$$

$$ln(\frac{n(t+\tau)}{n(t)}) = \int_{t}^{t+\tau} -S(t)dt \tag{M10}$$
$$= -\overline{S} \cdot \tau$$

It can be observed that Eq. M9 and Eq. M10 have similar formats with Eq. 2 and Eq. 4, only with $\overline{GR}$ and $\overline{S}$ instead of $GR$ and $S$, and $\tau$ instead of $t$.

Therefore, the assumption of constant $GR$ and $S$ (independent of time) is applicable to periods that are integer multiples of $\tau$ or periods much longer than $\tau$. This assumption cannot be used to describe BC mixing states during some fast and non-periodic meteorological condition changes (e.g., a passage of cold front and precipitation). When discussing the mixing state of BC, multi-day statistics are often adopted to represent its average condition, in which case the above derivation can be used. Moreover, the steady-state assumption is also applicable for us to determine the overall mixing state of BC on a large scale, which is one of our major targets in this study.

Light absorption enhancement:

As shown in Fig. S2, the relationship between $E_{abs}$ and $\Delta D_p$ is approximately linear when $\Delta D_p$ is small. Therefore, $E_{abs}$ could be represented as Eq. M11.

$$E_{abs}(D_c, \Delta D_p) = \alpha(D_c)\Delta D_p \tag{M11}$$

where $\alpha(D_c)$ is the linear coefficient of $E_{abs}$ and $\Delta D_p$. With the known calculation formula of $\overline{D_p}$, we can derive that

$$\overline{\Delta D_p} = \frac{\int_{D_p=D_c}^{\infty} D_p \cdot n(D_p) \cdot d(D_p)}{\int_{D_p=D_c}^{\infty} n(D_p) \cdot d(D_p)} = \frac{1}{k} \tag{M12}$$

The average $E_{abs}$ with given $D_c$ is found to be

$$E_{abs}(D_c) = \frac{\int_{D_p=D_c}^{\infty} c_{abs-external}(D_c) \cdot E_{abs}(D_c, \Delta D_p) \cdot n(D_c, D_p) \cdot d(D_p)}{\int_{D_p=D_c}^{\infty} c_{abs-external}(D_c) \cdot n(D_c, D_p) \cdot d(D_p)}$$

$$= \alpha(D_c) \cdot \overline{\Delta D_p} \qquad\qquad (M13)$$

$$= \alpha(D_c) \cdot \frac{1}{k}$$

$$= E_{abs}(D_c, \overline{\Delta D_p})$$

where $c_{abs-external}$ represents the light absorption coefficients of BC core. Eq. M12 and Eq. M13 shows that $1/k$ plays a similar role with coating thickness.

5

Field observations and site descriptions:

Observational data of BC mixing states was collected from different sites distributed in Nanjing (a regional background site in the Yangtze River Delta region in China), Beijing (an urban site in the capital of China), Shaoguan (a regional background site in the Pearl River Delta region in China), the Tibetan Plateau (include three sites with different features), Japan (Tokyo), and the United States (Sacramento, influenced by biomass burning).

Field measurements in Nanjing were performed at the Station for Observing Regional Processes of the Earth system (SORPES, 118°57′10″E, 32°07′14″ N; 40 m a.s.l.), a regional background station in the western YRD region. Detailed description of SORPES can be found in previous studies (*36*, *37*). Due to its geographical position, this observation platform is ideal to capture the transport from megacities in the YRD region and North China Plain. Observational data from February 2020, April 2020, and December 2021 was used in this study.

Observations in Lulang and Maqu were made over the Tibetan Plateau (TP) from April to July 2021. The Lulang site is located on the southeastern part of the TP with a few traffic emissions nearby. The measurement period in Lulang was from 1 April to 25 May 2021. Maqu can be considered as a background site over the TP. The measurement period was from 26 June to 8 July 2021. The observation locations and periods at other sites are summarized in Table S1.

25

Besides field observations conducted in this study, observational data from several sites covering different kinds of environment globally was also collected to support our findings. The measurement periods in Shaoguan, Beijing (*29*), Tokyo (*28*), Sacramento (*9*), and the Amazon Tall Tower Observatory (ATTO) were December 2020, November 2014, August 2012, June 2010, and October 2019, respectively. Shaoguan is a regional background site in southeastern China and Beijing site represents a heavily polluted region in the North China Plain. Tokyo and Sacramento sites are located in urban areas in Japan and the United States, respectively. The selected observation period at ATTO site covers a biomass burning episode including some relatively clean days. Detailed information on these observations is summarized in Table S1.

35

The physical properties of refractory BC particles were measured using a single particle soot photometer (SP2, Droplet Measurement Technologies, USA). The operation principle of the SP2 has been well described in previous literature (*20*, *38*). Briefly, sampled particles pass through a 1064 nm Nd:YAG laser beam. BC-containing particles heat up to their boiling point and incandesce. The BC mass can be computed based on its proportional relationship with the peak intensity of the incandescence signal and the BC mass equivalent diameter can be calculated with the known density of BC (normally assumed to be 1.8 g cm$^{-3}$ (*39*)). The scattering calibration was performed using polystyrene latex spheres (PSL). The rBC mass was calibrated using fullerene soot with known diameter, which was selected by a differential mobility analyzer (DMA, TSI Inc., USA) and its mass was calculated using effective density values presented by Gysel et al. (*40*). The leading-edge-only (LEO) fit method developed by Gao et al. (*20*) was adopted to calculate the scattering cross-section of BC-containing particles and saturated scattering particles. Therefore, the optical diameters of BC-containing particles can be further determined based on core-shell Mie theory.

Model simulations:

**Optical module in CAM6 and WRF-Chem:** There are two typical methods that are extensively applied for optical calculations in global climate models and regional transport models, i.e., the volume-mixing and core-shell Mie methods. The volume-mixing Mie algorithm assumes that all components are mixed in all individual particles and the mean refractive index is calculated as the volume-weighted average of the refractive indices of each species. The core-shell Mie method assumes that BC is in the center, and other components are coated on the BC core. The shell refractive indices are assumed to be the volume-weighted average of the refractive indices of dissolved components. The volume-mixing Mie algorithm is included in CAM6. Both volume-mixing and core-shell Mie methods can be used to estimate aerosol optical properties in WRF-Chem. The refractive indices for shortwave radiation and densities of aerosol species in CAM6 and WRF-Chem model are summarized in Table S3. $E_{abs}$ is the ratio of $MAC_{internal}$/$MAC_{external}$, where MAC stands for the mass absorption cross section of BC. Since there is no external mixing module in CAM6 and WRF-Chem, the estimation of $MAC_{external}$ is based on off-line calculation. The default refractive indices and densities in each model are adopted. The BC diameter is assumed to follow a lognormal distribution with a count median diameter of 70 nm (*2*).

The new mixing state and optical scheme based on our theory frame is established and applied in both CAM6 and WRF-Chem, which cover different model types. CAM6 and WRF-Chem are examples of global climate models and regional transport models, respectively. Moreover, CAM6 uses a modal aerosol module and WRF-Chem uses a sectional aerosol module, which are the two most widely implemented modules in atmospheric models. In the new scheme, a monodisperse coating thickness of 70 nm derived from k=0.014 is adopted. In CAM6 and WRF-Chem, the BC core diameter is assumed to follow a lognormal distribution with a count median diameter of 70 nm.

**CAM6:** We used the Community Atmosphere Model version 2.1.3 of the Community Earth System Model version 6 (CESM2.1.3-CAM6) in the simulation of light absorption by BC and the global DRF with Modal Aerosol Module 4 (MAM4). MAM4 includes six aerosol components (BC, sea salt, sulfate, POA, SOA, and dust), which are divided into four modes (primary carbon mode, Aitken mode, accumulation mode and coarse mode), and simulates the mass mixing ratios

of six components within each mode. The spatial resolution in the global simulation is $1.9^{\circ} \times 2.5^{\circ}$ for a latitude and longitude grid with 70 vertical layers (from 50 m to ~ 140 km). The simulation is performed for four years (2012 ~ 2015) with the spin-up in the first year and analysis in the last three years. The radiative transfer module in the shortwave is calculated by the radiation code RRTMG. The diagnostic calculation of CAM6 is conducted for the radiative properties of one specific component, namely by double running case with and without that component. The aerosols in the accumulation mode in this study are resolved with a sectional representation (30 size bins) in the optical calculations.

The BC-induced direct radiative forcing ($DRF_{BC}$) in the conventional models is simulated using the default setting. The $DRF_{BC}$ determined with our new module by using $k$ is performed assuming $DRF_{BC}$ is linear with MAC (2, 41). Thus, the $DRF_{BC\_k}$ can be estimated from the change of $MAC_k$ and MAC in CESM.

**WRF-Chem:** WRF-Chem version 3.7 (Weather Research and Forecasting model coupled with Chemistry) was employed in this study, which is an online-coupled meteorology and chemistry model considering multiple physical and chemical processes, including emission and deposition of pollutants, advection and diffusion, gaseous(42) and aqueous chemical transformation, aerosol chemistry, and dynamics (43). The model has been incorporated in several studies concerning the estimation of aerosol optical properties and its radiative forcing (44, 45). The model domain is centered at 35.0 ºN, 110.0 ºE with a grid resolution of 20 km that covers eastern China and the surrounding regions. A total of 30 vertical layers extending from the surface to 50 hPa are utilized in the model. The simulation is conducted for the first two weeks of April 2020, and each run covers 36 h and the last 24 h of output were kept for further analysis. The initial and boundary conditions of meteorological fields were updated from the 6-hour NCEP (National Centers for Environment Prediction) global final analysis (FNL) data with $1^{\circ} \times 1^{\circ}$ spatial resolution. The Rapid Radiative Transfer Model shortwave and longwave radiation scheme (RRTMG) represents the radiation transfer within the atmosphere (46). Anthropogenic emissions from power plants, residential combustion, industrial processes, on-road mobile sources, and agricultural activities were derived from the MIX Asian emission inventory database (47). Emissions of major pollutants such as carbon monoxide, sulfur dioxide, nitrogen oxides, ammonia, and speciated VOCs are all included. The MEGAN (Model of Emissions of Gases and Aerosols from Nature, version2) model embedded in WRF-Chem is used to calculate biogenic emissions online. Soil derived dust emissions are characterized by the GOCART emission schemes. For numerical representation of atmospheric chemistry, we used the CBMZ (Carbon-Bond Mechanism version Z) photochemical mechanism combined with the MOSAIC (Model for Simulating Aerosol Interactions and Chemistry) aerosol model (48). Major aerosol components include black carbon (BC), organic mass, sulfate, nitrate, ammonium, and other inorganic species. All aerosols were assumed to be spherical particles. The size distribution was divided into four discrete size bin defined by their lower and upper dry particle diameters (0.039-0.156, 0.156-0.625, 0.625-2.5, 2.5-10.0 μm). In each bin, aerosols were assumed to be internally mixed.
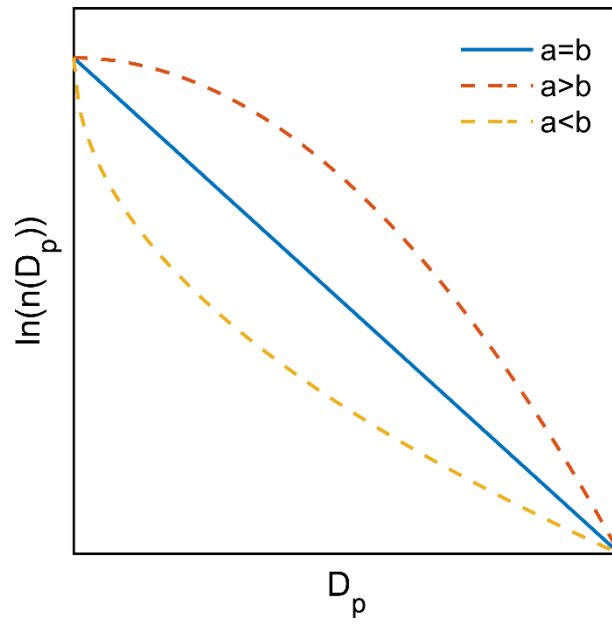
**Fig. S1. Theoretical relationship between *ln(n(D$_p$))* and *D$_p$* under three conditions.** The blue line represents the case demonstrated in the main text.
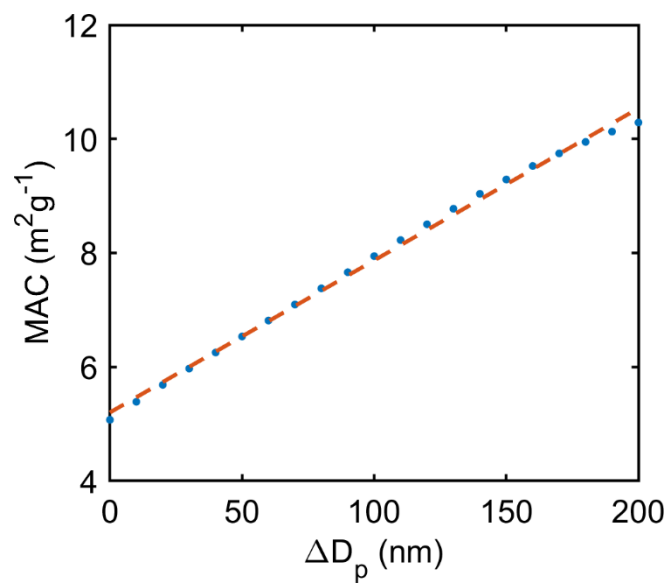
**Fig. S2. Change of mass absorption cross-section (MAC) of BC with $\Delta D_p$.** Blue dots represent the calculated MAC based on core-shell Mie theory with linear fit shown as the red line.
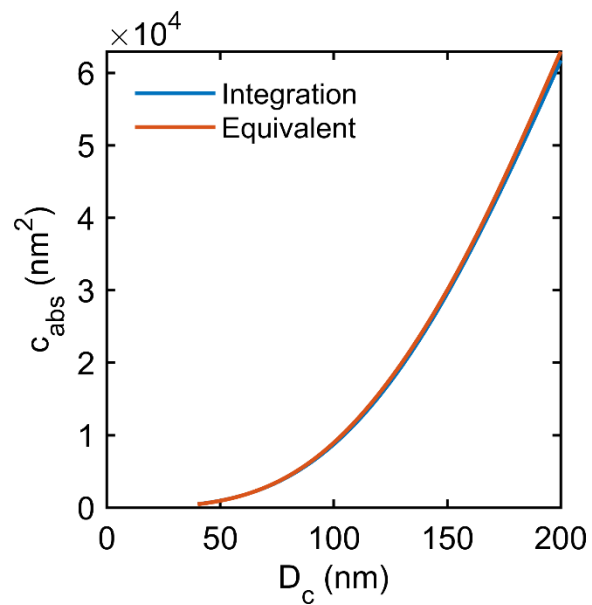
**Fig. S3. BC absorption coefficient calculated using equivalent $D_p$ and $D_p$ distributions.** Red line represents calculated $c_{abs}$ using equivalent $D_p$. Blue line stands for calculated $c_{abs}$ using integrated $D_p$ from $D_p$ distribution.

**Table S1.**

Observation period and site type for SP2 measurements

| Site | Observation period | Type | Reference |
|---|---|---|---|
| Nanjing, China | 1/2/2020–28/2/2020 1/4/2020–30/4/2020 1/12/2021–31/12/2021 | Suburban | This study |
| Lulang, China | 1/4/2021–25/5/2021 | Background in TP | This study |
| Maqu, China | 26/6/2021–8/7/2021 | Rural in TP | This study |
| Shaoguan, China | 4/12/2020–10/12/2020 | Rural | This study |
| Beijing, China | 13/11/2014–3/12/2014 | Urban | Zhang et al., 2018 (*3*) |
| Sacramento, USA | 14/6/2010–15/6/2010 | Urban with biomass burning influence | Zaveri et al., 2012 (*24*) |
| Tokyo, Japan | 2/8/2012–8/8/2012 | Urban | Moteki et al, 2014 (*28*) |
| ATTO, Brazil | 23/10/2019–31/10/2019 | Biomass burning | |

5

**Table S2.**

$E_{abs}$ of BC from field observation.

| Longitude Latitude | Location | Wavelength (nm) | Sampling duration | $E_{abs}$ | References |
|---|---|---|---|---|---|
| 43.66°N 79.39°W | Toronto Canada | 760 | 2006.12-2007.1 | 1.21 [1.02-1.43][#] | Knox et al., 2009 (*31*) |
| 38.64°N 121.35°W | Sacramento, USA | 405 | 2010.6.17-2010.6.29 | 1.13±0.01 | Cappa et al., 2012 (*9*) |
| | | 532 | | 1.06±0.006 | |
| 40.02°N 105.27°W | Boulder USA | 404 | 2010.9 | 1.5 | Lack et al., 2012 (*32*) |
| | | 532 | | 1.3 | |
| 51.05°N 0.12°W | London UK | 405 | 2012.2 | 1.3 | Liu et al., 2015 (*13*) |
| | | 781 | | 1.4 | |
| 37.50°N 137.40°E | Noto Penin-sula, Japan | 405 | 2013.4.17-2013.5.14 | 0.99 [0.87-1.06][*] | Ueda et al., 2016 (*33*) |
| | | 532 | | 1.06 [0.93-1.20][*] | |
| | | 781 | | 1.23 [1.10-1.35][*] | |
| 32.06°N 118.70°E | Nanjing, China. | 405 | 2014.8.16-2014.8.28 | 1.41±0.39 | Ma et al., 2020 (*35*) |
| | | 532 | | 1.42±0.40 | |
| | | 781 | | 1.35±0.38 | |
| 36.81°N 119.78°W | Fresno, USA | 405 | 2014.12.25-2015.1.12 | 1.37±0.22 | Cappa et al., 2019 (*34*) |
| | | 532 | | 1.22±0.15 | |
| | | 870 | | 1.10±0.13 | |
| 34.10°N 117.49°W | Fontana USA | 405 | 2015.7.3-2015.7.15 | 1.10±0.27 | Cappa et al., 2019 (*34*) |
| | | 532 | | 1.07±0.22 | |

Measured $E_{abs}$ using thermodenuder (TD) method was listed in above table. TD method removes coating material by heating the sample in a TD, then defined $E_{abs}$ with $E_{abs} = b_{abs;ambient}/b_{abs;TD}$, where $b_{abs;TD}$ is corrected for particle losses.

[#]$E_{abs}$ in Knox et al., 2009 (*31*) was obtained from $MAC_{unheated}/MAC_{heated}$. The range represents the $E_{abs}$ of aerosol with different age category.

[*]$E_{abs}$ range was the 25th-75th percentile.

**Table S3.**

Densities and refractive indices for shortwave radiation of the species in CAM6 and WRF-Chem simulations.

| Species | Density (g cm$^{-3}$) (CAM6) | Density (g cm$^{-3}$) (WRF-Chem) | Refractive index (CAM6) | Refractive index (WRF-Chem) |
|---|---|---|---|---|
| Black carbon | 1.7 | 1.8 | 1.95 + 0.79i | 1.85 + 0.71i |
| Organic matter | 1.0 | 1.0 | 1.53 + 0.0057i | 1.45 + 0i |
| Dust | 2.6 | 2.6 | 1.56 + 0.0019i | 1.55 + 0.003i |
| Sulfate | 1.77 | 1.8 | 1.43 + 0i | 1.45 + 0i |
| Nitrate | 1.77 | 1.8 | 1.5 + 0i | 1.45 + 0i |
| Ammonia | 1.77 | 1.8 | 1.5 + 0i | 1.45 + 0i |

5